Design of Fe3–xO4 raspberry decorated graphene nanocomposites with high performances in lithium-ion battery

Olivier Gerber, Sylvie Bégin-Colin, Benoit P. Pichon, Elodie Barraud, Sébastien Lemonnier, Cuong Pham-Huu, Barbara Daffos, Patrice Simon, Jérémy Come, Dominique Bégin

j

Design of $Fe_{3-x}O_4$ raspberry decorated graphene nanocomposites with high performances in lithium-ion battery☆

Olivier Gerber[a,c], Sylvie Bégin-Colin[a], Benoit P. Pichon[a], Elodie Barraud[c], Sébastien Lemonnier[c], Cuong Pham-Huu[d,*], Barbara Daffos[b], Patrice Simon[b], Jeremy Come[b,**], Dominique Bégin[d,***]

[a] Institut de Physique et Chimie des Matériaux de Strasbourg, UMR 7504 - CNRS, Université de Strasbourg, 23 rue du Loess, 67034 Strasbourg Cedex 08, France
[b] RS2E - FR CNRS n 3459, Université Paul Sabatier, Toulouse III, CIRIMAT, 118 route de Narbonne, 31062 Toulouse Cedex 9, France
[c] French–German Research Institute of Saint-Louis, 5 rue du Général Cassagnou, 68300 Saint-Louis, France
[d] Institut de Chimie et Procédés pour l'Energie, l'Environnement et la Santé, UMR 7515-CNRS, Université de Strasbourg, 25 rue Becquerel, 67087 Strasbourg Cedex 02, France

A B S T R A C T

$Fe_{3-x}O_4$ raspberry shaped nanostructures/graphene nanocomposites were synthesized by a one-step polyol-solvothermal method to be tested as electrode materials for Li-ion battery (LIB). Indeed, $Fe_{3-x}O_4$ raspberry shaped nanostructures consist of original oriented aggregates of $Fe_{3-x}O_4$ magnetite nanocrystals, ensuring a low oxidation state of magnetite and a hollow and porous structure, which has been easily combined with graphene sheets. The resulting nanocomposite powder displays a very homogeneous spatial distribution of $Fe_{3-x}O_4$ nanostructures at the surface of the graphene sheets. These original nanostructures and their strong interaction with the graphene sheets resulted in very small capacity fading upon Li^+ ion intercalation. Reversible capacity, as high as 660 mAh/g, makes this material promising for anode in Li-ion batteries application.

Keywords:
Graphene
$Fe_{3-x}O_4$ raspberry shaped nanostructures
$Fe_{3-x}O_4$/graphene nanocomposites
Lithium-ion battery
Reversible capacity

1. Introduction

Lithium-ion batteries (LIBs) are widely used in portable electronic devices, and show increasing interest for powering electric vehicles [1]. To date, most of commercial LIBs use graphite as negative electrode thanks to its low discharge plateau and cycling stability [1–4]. However, graphite specific capacity is limited to 372 mAh/g upon Li^+ intercalation, and exhibits poor rate performance associated with the risk of metallic Li deposition at high charging regimes [1,5]. To meet the demand in high energy and high power electrochemical storage devices, alternative anode materials have been investigated [6,7], including alloying reaction metals [8], or conversion reaction oxides [9–11]. Among them, spinel iron oxide Fe_3O_4 has been considered as a promising oxide thanks to its high theoretical capacity of 924 mAh/g, its environmental benign, large abundance and low cost [5,6,9,12–16]. Moreover, Fe_3O_4 shows a potential around 1 V versus Li^+/Li, which provides better safety versus metallic Li deposition at high rate. However these applications are limited by poor cycling performance arising from the structure breakdown linked with volume change during the electrochemical reaction with Li, as well as important polarization during the charge/discharge processes [5,15,17,18]. To increase the number of cycles, various approaches have been proposed such as carbon based coating [15,19], electrodes nanostructuring [11,16,17,20], or nanocomposites [5,18,21]. Taberna et al. proposed to attach Fe_3O_4 nanoparticules onto nanostructured copper foil by electrodeposition [11] but the best performances were obtained using carbon-based composites such as carbon shells, carbon nanotubes, or graphene [16,22–24]. Besides, $Fe_{3-x}O_4$ nanostructures, consisting of aggregates of nanocrystals, have shown interesting performances as electrode material [25,26] but the low electronic conductivity of iron oxide leads to poor rate performance and they require thus the addition of non-electroactive material such as acetylene black.

Graphene and few-layer graphene (FLG) materials have received an ever increasing scientific interest during the last decades thanks

☆ This work was supported by the funding from the European Research Council (ERC, Advanced Grant, ERC-2011-AdG, Project 291543-IONACES). The authors also acknowledge the funding from the Materials Institute Carnot Alsace (MICA) and from the Direction Générale de l'Armement (DGA) and French-German Research Institute of Saint-Louis (ISL).

* Corresponding authors.
E-mail addresses: cuong.pham-huu@unistra.fr (C. Pham-Huu), jeremy0come@gmail.com (J. Come), dominique.begin@unistra.fr (D. Bégin).

http://dx.doi.org/10.1016/j.jechem.2016.01.021

to their exceptional physical properties [27–30]. These 2D materials can be synthesized by different methods such as micromechanical alleviation of graphite, liquid-phase exfoliation, mechanical ablation, high-temperature treatment of silicon carbide, catalytic or chemical unzipping of carbon nanotubes as well as chemical vapor deposition (CVD) or by reduction of graphene oxide (GO) [31–36]. In the LIB application, it is expected that graphene and FLG could play a significant role to stabilize deposited transition metal oxides, improving the electrical conductivity of the composite and voids for accommodating volume change during the charge/discharge cycles.

We recently synthesized nanohybrid materials combining metal oxide nanoparticles (M = Co or Fe) with an extremely narrow size distribution and carbon nanotubes [37,38] or few-layer graphene (FLG) [39] with a metal oxide content up to 50%. Iron oxide nanoparticles with mean diameter ranged from 5 to 50 nm (depending on the synthesis conditions) were well dispersed on both side of the FLG surface, according to the recent TEM tomography analysis [40]. These nanoparticles further act as spacers to prevent the complete restacking of the FLG through van der Walls forces.

Using a similar approach, porous $Fe_{3-x}O_4$ hollow nanostructures with a raspberry shape, narrow size distribution, well-defined chemical composition and crystalline structure [30] were successfully grown onto few-layer graphene sheets with highly controlled covering density. These nanostructures consist of oriented aggregates of magnetite nanocrystals (nanocrystals with common crystallographic orientations directly combined together to form larger ones) which ensure a nanostructuration, porosity and a low oxidation state of Fe_3O_4 nanocrystals [41]. The structure of such a composite presents several interests for electrode material such as (i) a high porosity that provides both high electrode/electrolyte interface area and fast Li^+ diffusion path toward active reaction sites, (ii) a preservation of the magnetite composition at low nanocrystal sizes (as described in ref. [30]) that improves the capacity performance, and (iii) a highly conductive graphene matrix that provides an excellent interface with the $Fe_{3-x}O_4$ nanostructures and ensures high electronic percolation without the need of conducting additives, and (iv) the strong interaction between the iron oxide and the graphene surface which significantly reduces the problem of deactivation linked with the excessive sintering of the iron oxide compounds upon LIB experiments. The 2D morphology of the FLG also contributes to the flexibility of the composite as a function of charge/discharge cycle and to prevent the breaking of the composite structure for long-term operation.

In this work, we report on the use of these $Fe_{3-x}O_4$ raspberry shaped nanostructures deposited on graphene sheets (synthesized by an "ultimate" exfoliation of expanded graphite), as anode material for LIB application. The composite demonstrates specific capacity values as high as 660 mAh/g at 8 C with excellent cycling stability. The samples, before and after LIB tests, were also characterized by different techniques in order to get more insight about the possible structural modification during the charge/discharge cycling and also for subsequence optimization process.

2. Experimental

2.1. Graphene and few-layer graphene synthesis

Few-layer graphene (FLG) powders were obtained using a technique derived from the synthesis developed by Janowska et al. based on an "ultimate" exfoliation of graphite-based material or expanded graphite [42,43]. The expanded graphite powder Carbon Lorraine was dispersed in ethanol by an ultrasonic treatment (finger) during 30 min: ultrasonic finger is a "Branson" instrument (Digital sonifier 450) with a maximal power of 400 W (in reality 20% to 40% of the maximal power was used). After the solution containing the powder was decanted for 1 h, the supernatant solution containing the smaller particles was collected and the operation was repeated two times to obtain the few-layer graphene powder.

2.2. Synthesis of $Fe_{3-x}O_4$@graphene hybrid nanostructure

The $Fe_{3-x}O_4$@graphene was synthesized by a one-step mixed polyol-solvothermal method. In a typical synthesis, iron chloride hexahydrate (1.00 mmol), succinic acid (0.33 mmol), urea (10.0 mmol) and a given amount of graphene (10.0 mg, 20.0 mg and 100.0 mg) were dispersed in ethylene glycol (10.0 mL) by vigorous mechanical stirring and ultrasonication. The solution was subsequently sealed in a Teflon lined stainless steel autoclave (20 mL volume), slowly heated at 200 °C for 4 h and maintained at this temperature for 10 h. After cooling down to room temperature, the precipitated powder was separated by centrifugation and was then washed several times using deionized water and ethanol. Finally, the powder was freeze dried before characterizations. Samples were named NC-10, NC-20 and NC-100 accordingly to the amount of graphene used.

2.3. Structural characterizations

Scanning electron microscopy (SEM) analysis was carried out on a JEOL 6700F microscope working at 10 kV accelerated voltage. Transmission electron microscopy (TEM) was carried out using a JEOL 2100F (voltage 200 kV) microscope with a point resolution of 0.2 nm. The sample was dispersed in ethanol by ultrasonication during 5 min and a drop of the solution was then deposited on a copper grid (covered with a carbon membrane). X-ray diffraction (XRD) was carried out using a Bruker D8 Advance in the 27°–75° (2θ) range with a scan step of 0.03°. The detector was a three degrees wide analysis detector ("Lynx Eye"). Thermal gravimetric analyses were carried out with a TA Instrument (Q-5000 model). They were performed under an air flow (20 mL/min) up to 1000 °C with a heating rate of 5 °C/min. The specific surface area was determined with a Micromeritics sorptometer (Tristar). The sample was outgassed at 250 °C under vacuum for 12 h in order to desorb moisture and adsorbed species on its surface. The measurements were carried out using N_2 as adsorbent at liquid N_2 temperature.

2.4. Electrochemical characterizations

2-electrode Swagelok cells were assembled in an argon-filled glove box using the nanocomposite powder as the positive electrode and the Li metal as the negative electrode. A Whatman GF/B borosilicate glass-fiber (520 μm-thick) saturated with 1 M $LiPF_6$ electrolyte solution (in EC : DMC=1 : 1 in volume ratio) was used as the separator. Powders were used without any conducting additives. The electrode loading was between 2 and 2.5 mg/cm^2. All measurements were carried out using a Bio-Logic WMP 3 potentiostat, between 0.05 and 3 V (versus Li/Li^+). The rate performance was obtained by the so-called “signature” experiment as described in details in the reference [11].

3. Results and discussions

Fig. 1(a–d) shows SEM images of the graphene/$Fe_{3-x}O_4$ nanocomposites with three different weight ratios raspberry $Fe_{3-x}O_4$ nanostructures/graphene (1 for NC-100, 5 for NC-20 and 10 for NC-10). The mean $Fe_{3-x}O_4$ nanostructure size is centered to 250 nm and is very similar for all three samples meaning that the amount of graphene does not affect the formation of iron oxide nanostructures. They consist of original orientated aggregates of $Fe_{3-x}O_4$ nanocrystals (Fig. 1e) with a mean size of 25 nm, mainly

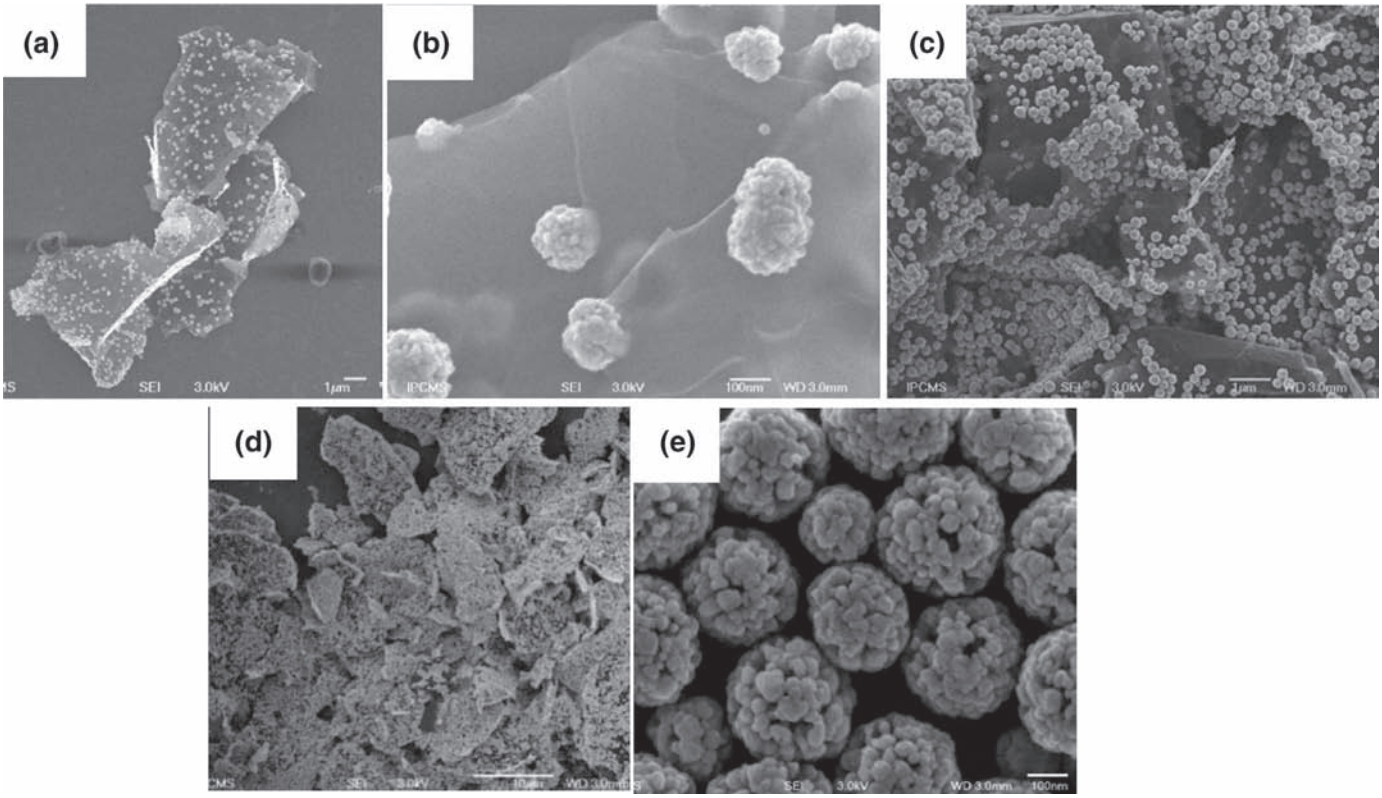

Fig. 1. SEM images of $Fe_{3-x}O_4$/graphene sheets nanocomposites with different weight ratios $Fe_{3-x}O_4$/graphene: NC-100 (a,b), NC-20 (c) and NC-10 (d) and of isolated nanostructures showing $Fe_{3-x}O_4$ aggregates constituted by assembly of several nanocrystals (e).

constituted of the magnetite phase ($Fe_{2.90}O_4$, 70% of magnetite) and exhibiting a porous and hollow structure with a BET specific surface area of 27 m^2/g [41]. The spatial distribution of nanostructures onto the graphene sheets is relatively homogeneous for all nanocomposites, with higher volumetric mass density for the sample with low amount of graphene (Fig. 1a–d). Such strong interactions may be attributed to the nucleation-growth of nanostructures from defects and/or steps onto graphene sheets (Fig. 1b) [39]. It is also worthy to note that the synthesis is extremely selective for preparing $Fe_{3-x}O_4$ aggregated nanostructures with controlled size as high-resolution SEM micrograph (Fig. 1e) clearly shows.

The strong interaction between nanostructures and graphene sheets, especially the graphene sheet border, is clearly visible on the edges where nanostructures "marry" the shape of the sheet (Fig. 2a). According to these results, one can state that the iron oxide nucleation also started at the defect sites localized on the border of the graphene sheets where sites with high reactivity are present. The high reactivity of the border sites on the FLG has already been reported by other research groups in the literature showing the decoration of the graphene border with subnanometer platinum clusters [44,45]. High resolution SEM micrograph also evidences the formation of iron oxide aggregates with different morphology on the FLG surface (Fig. 2b). Indeed, despite a large part of the iron oxide aggregates are in a round-shaped form, the SEM micrograph also reveals the presence of some other iron oxide aggregates with a hemi-sphere shape on the edge sites of the FLG (indicated by arrows) which strongly confirms the high interaction between the deposited iron oxide aggregates and the FLG surface.

The microstructure of the $Fe_{3-x}O_4$ aggregates, well dispersed on a high surface area alumina support in order to avoid the overlapping, was also analyzed by TEM and the representative TEM micrographs are presented in Fig. 3. The TEM results confirm the homogeneous size of the iron oxide aggregates (Fig. 3a) while high-resolution TEM clearly evidences the presence of $Fe_{3-x}O_4$ nanoparticles within the aggregate (Fig. 3b). It is expected that such iron oxide nanoparticle assembly will provide an "easy access" for the lithium ion insertion while the hollow structure of the aggregate allows the composite to resist to the expansion consecutive to the lithium insertion.

TGA curves (Fig. 4a) have shown that theoretical and experimental carbon/$Fe_{3-x}O_4$ weight ratios are very close which confirms the high efficiency of the synthesis method for decorating the FLG surface with controlled size of iron oxide nanostructures. Its variation between 2 and 0.1 is perfectly correlated to the amount of carbon added in the reaction medium. X-ray diffraction pattern (Fig. 4b) confirms that the iron oxide aggregated nanostructures are constituted of the spinel iron oxide with a composition very close to that of the magnetite phase (JCPDS 19-0629).

3.1. Electrochemical characterizations of nanocomposites in Li-ion cells

The NC-100 nanocomposite has been found to be the most efficient as anode material in Li-ion device. Fig. 5 shows the Cyclic Voltammograms (CVs) of NC-100 in 1 M $LiPF_6$ in EC : DMC (1 : 1 in volume ratio) electrolyte at 0.2 mV/s. Starting from the Open Circuit Voltage (OCV) at 2.9 V versus Li down to 0.1 V versus Li, the first cycle shows a slight reduction peak at 1.5 V versus Li and an important redox peak at 0.55 V versus Li. The small peak at 1.5 V is associated with the structure transition caused by Li insertion into Fe_3O_4 ($Fe_3O_4 + xLi^+ + xe^- \rightarrow Li_xFe_3O_4$). The peak at 0.55 V versus Li corresponds to the further transformation of $Li_xFe_3O_4$ into metallic Fe through the conversion reaction ($Li_xFe_3O_4 + (8-x)Li^+ + (8-x)e^- \rightarrow 4Li_2O + 3Fe$), together with the formation of the SEI layer on the graphene/Fe_3O_4 electrode [33]. From 0.2 V down to 0.1 V

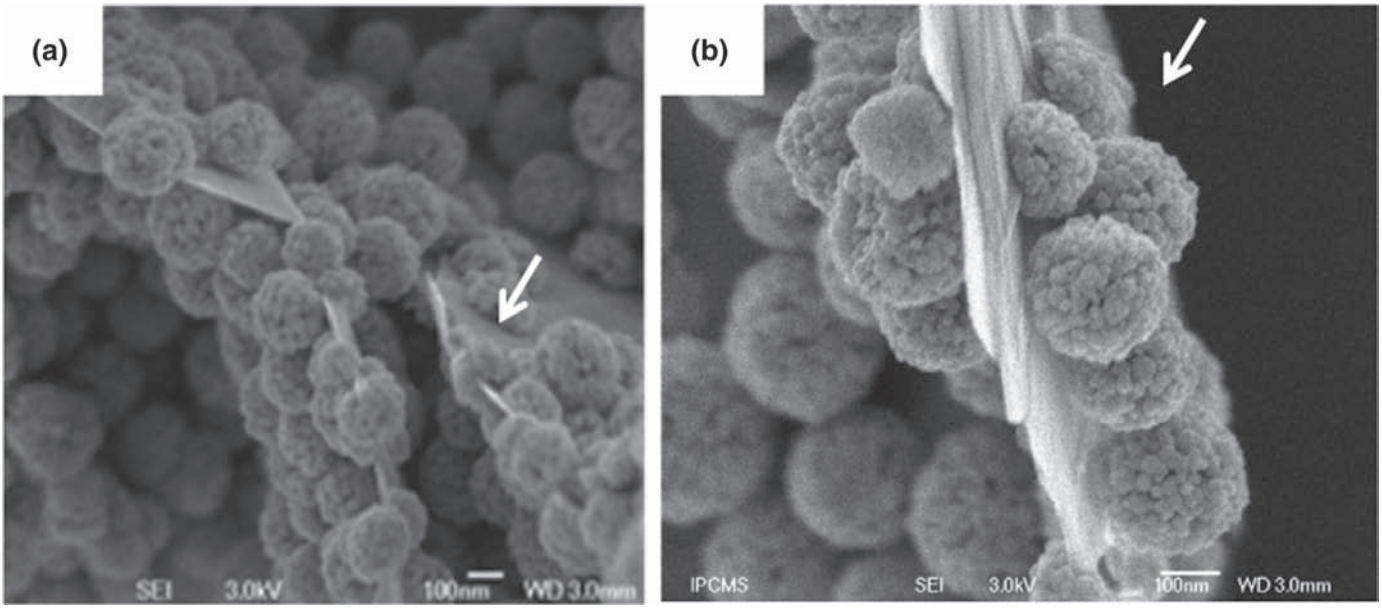

Fig. 2. High resolution SEM micrographs of the nanostructure/FLG composite showing the anchorage of the iron oxide aggregates on both side of the graphene sheet and also the presence of strong oxide/support interaction leading to the formation of iron oxide hemispheres aggregates (indicated by arrows).

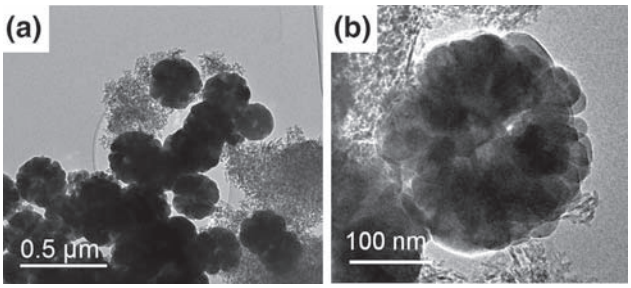

Fig. 3. TEM analysis of the $Fe_{3-x}O_4$ nanostructures showing the presence of $Fe_{3-x}O_4$ nanoparticles with diameter ranged between 30 mm and 70 nm within the aggregate.

versus Li, the reversible intercalation of Li ions into graphene layer scan be seen, according to $2C + Li^+ + e^- \rightarrow LiC_2$ [34].

During positive scan (oxidation), the Li de-insertion is visible at 0.2 V versus Li. The peaks at 1.68 V and 1.89 V versus Li correspond to the reverse of the reduction reaction that is the oxidation of metallic Fe into Fe^{2+} and Fe^{3+}, respectively. The shift in the peak potentials between the first and subsequent cycles originates from the thermodynamics of the conversion reaction [11].

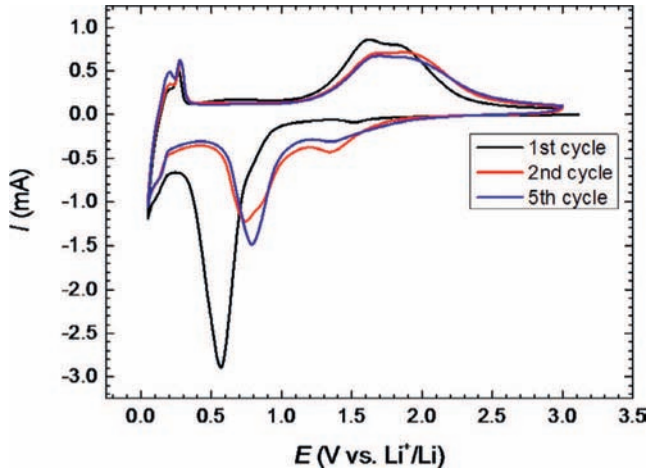

Fig. 5. Cyclic voltammograms of the Fe_3O_4 raspberry/graphene sheets in 1 M $LiPF_6$ in EC: DMC (1: 1 in volume ratio) electrolyte, at 0.2 mV/s.

Fig. 6 shows the galvanostatic charge/discharge plots obtained for the NC-100 containing 50 wt% of $Fe_{3-x}O_4$ at 1 C rate. The first cycle starts with the Li insertion into Fe_3O_4 ($Fe_3O_4 + xLi^+ + xe^- \rightarrow Li_xFe_3O_4$) at 1.5 V, before reaching the conversion

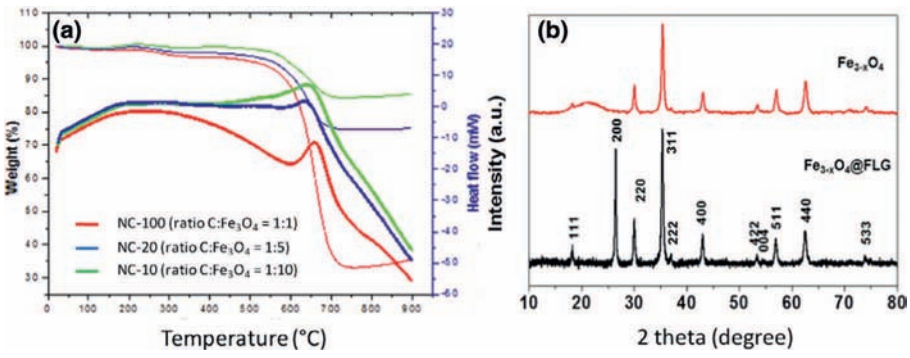

Fig. 4. (a) TG-DTA curves of NC-100, NC-20 and NC-10 and (b) XRD pattern of NC-10 (This XRD pattern is characteristic of those of all composites).

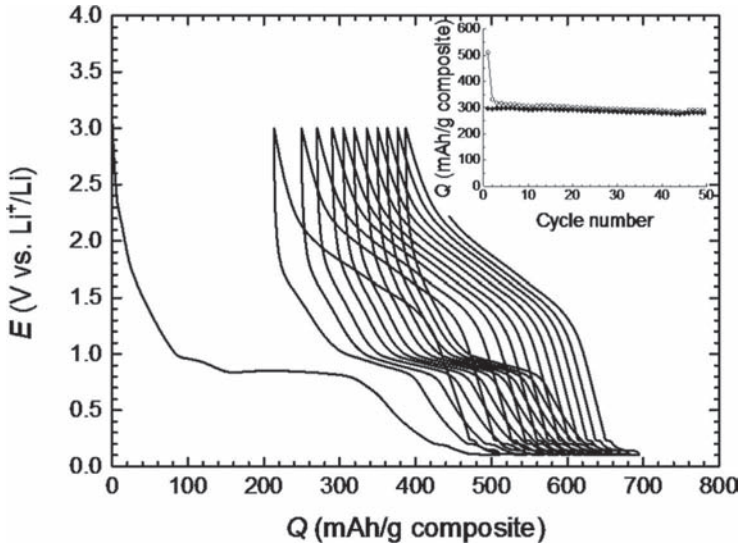

Fig. 6. Galvanostatic charge/discharge plots for the $Fe_{3-x}O_4$ nanostructures/graphene sheets containing 50 wt% of $Fe_{3-x}O_4$, at 1 C rate.

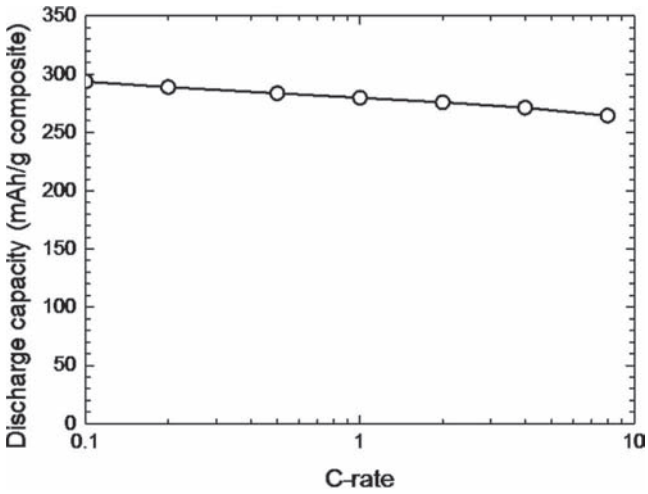

Fig. 7. Power plot for the Fe_3O_4 raspberry/graphene sheets containing 50 wt% of Fe_3O_4; details of the power plot construction is given in experimental section.

reaction of Fe_3O_4 down to metallic Fe ($Li_xFe_3O_4 + (8-x)Li^+ + (8-x)e^- \rightarrow 4Li_2O + 3Fe$) observed at 0.8 V; the end of the plateau and the slopping zone correspond to the SEI formation. Upon cycling, the well-known hysteresis associated with the conversion reaction is observed, that leads to an important polarization between charge and discharge.

The graphene/iron oxide nanocomposite shows a stable capacity behavior with cycles (inset Fig. 6). The capacity reaches 330 mAh/g on the composite basis weight which is accounted to 660 mAh/g for Fe_3O_4 (the capacity of graphene alone was measured and is negligible). Such a value is slightly below previous ones reported in the literature for magnetite or graphene/iron oxide composite materials [11,46,47]. However, the weight loading used here (2.5 mg/cm²) allows reaching a real capacity of 0.8 mAh/cm² that compares favorably to previous work. At this time, the values measured in the case of NC-10 and NC-20 are lower: the metal oxide/graphene weight ratio must be optimized to obtain a good electrical contact between the nanostructures and the graphene sheets.

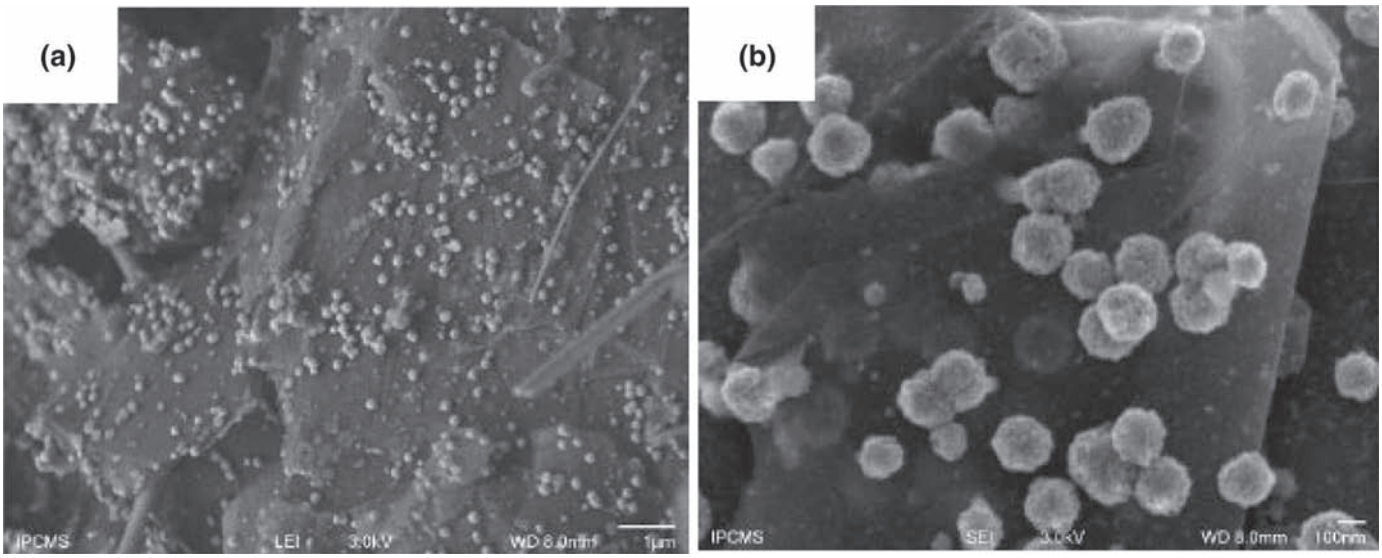

Fig. 8. SEM images of the raspberry nanostructures after 50 charge/discharge cycles showing the high stability of the iron oxide aggregates after charge/discharge cycles. Some sintering is observed as indicated by arrows.

The electrodes synthesized from NC-100 were able to discharge up to 8 C still keeping 90% of the capacity (Fig. 7), which evidence the high power performance of the electrodes, originating from the combination of the high conductivity of the graphene substrates and the $Fe_{3-x}O_4$ raspberry nanostructure constituted of iron oxide nanoparticles with smaller diameter (25 nm). The strong interaction between the iron oxide nanostructures and the FLG surface also prevents leaching and excessive sintering (see below) of iron oxide during the charge/discharge experiments. Such electrodes can be interesting in designing high power systems, while the energy density can be fine-tuned by controlling the Fe_3O_4 content in the composite.

Finally, after 50 charge/discharge cycles, the morphology of the raspberry nanostructures remains very similar according to the SEM analysis (Fig. 8). Such a high stability could be attributed to the strong interaction between the iron oxide aggregated nanostructures and the graphene surface which prevents excessive sintering during the LIB experiments. However, some local sintering can be observed in the SEM micrograph (Fig. 8b). It is expected that such sintering was somehow significantly reduced thanks to the strong interaction between the iron oxide aggregates and the graphene surface which prevent excessive motion of the iron oxide aggregates during the charge/discharge experiments.

4. Conclusions

$Fe_{3-x}O_4$ raspberry nanostructures/graphene nanocomposites have been synthesized by a one-step polyol-solvothermal method with Fe/C molar ratios varying from 1 to 10. Iron oxide nanostructures are distributed homogeneously on both side of the graphene sheets and acting as spacer to prevent the re-stacking of the graphene sheets through van der Walls attractions. The iron oxide nanostructures are strongly anchored on the graphene surface, through defect, vacancies and border/edge sites, and are present both in a round-shaped and hemispheres forms. The nanocomposite with the highest density on iron oxide nanostructures has been tested as anodes in Li-ion batteries and displays a reversible capacity, as high as 660 mAh/g, which makes this type of nanocomposite materials very promising for Li-ion battery applications. The relatively high and extremely stable charge/discharge of the Fe_3O_{4-x}/FLG could be attributed to several facts: the strong anchorage of the iron oxide aggregated nanostructures on the FLG which prevents the sintering during the LIB experiments, a porosity providing an easy path for lithium ion insertion and the high electrical conductivity of the graphene layer. The interconnected graphene structure in the composite also provides extra space to the volume change of the iron oxide nanostructures during the charge/discharge process. Work is underway to optimize the performance of such hybrid materials by introducing doping or by alloying the as-synthesized iron oxide with other oxides. It is also expected that the composite studied in the present work could be also useful for other applications in the field of heterogeneous catalysis, i.e. direct dehydrogenation or selective oxidation processes, where high mass transfer is key issue for the catalyst stability with improving selectivity.

Acknowledgments

The authors would like to thank Cedric Leuvrey (IPCMS, UMR 7504) and Walid Baaziz (ICPEES, UMR 7515) for SEM and TEM experiments.

References

[1] J.M. Tarascon, M. Armand, Nature 414 (2001) 359–367.
[2] M. Armand, J.M. Tarascon, Nature 51 (2008) 652–657.
[3] S. Flandrois, B. Simon, Carbon 37 (1999) 165–180.
[4] M. Endo, C. Kim, K. Nishimura, T. Fujino, K. Miyaita, Carbon 38 (2000) 183–197.
[5] Y. He, L. Huang, J.S. Cai, X.M. Zheng, S.G. Sun, Electrochim. Acta 55 (2010) 1140–1144.
[6] Y. Idota, T. Kubota, A. Matsufuji, Y. Maekawa, T. Miyasaka, Science 276 (1997) 1395–1397.
[7] J. Cabana, L. Monconduit, D. Larcher, M. Palacin, Adv. Mater. 22 (2010) E170–E192.
[8] C.K. Chan, H. Peng, G. Liu, K. McIlwrath, X.F. Zhang, R.A. Huggins, Y. Cui, Nat. Nanotechnol. 3 (1) (2008) 31–35.
[9] P. Poizot, S. Laruelle, S. Grugeon, L. Dupont, J.M. Tarascon, Nature 407 (2000) 496–499.
[10] H. Wang, L.F. Coi, Y. Yang, H.S. Casalongue, J.T. Robinson, Y. Liang, Y. Coi, H. Daï, J. Am. Chem. Soc. 132 (2010) 13978–13980.
[11] P.L. Taberna, S. Mitra, P. Poizot, P. Simon, J.M. Tarascon, Nat. Mater. 5 (2006) 67–574.
[12] J. Chen, L. Xu, W. Li, X. Gou, Adv. Mater 17 (2005) 582–586.
[13] B.Song Y.Chen, X. Tang, T. Lu, J. Xue, J. Mater. Chem 22 (2012) 17656–17662.
[14] T. Yoon, C. Chae, Y.K. Sun, H.H. Kung, J.K. Lee, J. Mater. Chem 21 (2011) 1725–1730.
[15] W.M. Zhang, X.L. Wu, J.S. Hu, Y.G. Guo, L.J. Wan, Adv. Funct. Mater. 18 (2008) 3941–3946.
[16] P. Liana, X. Zhub, H. Xianga, Z. Li, W. Yang, H. Wang, Electrochimca Acta 56 (2010) 834–840.
[17] T. Muraliganth, A.V. Murugan, A. Manthiram, Chem. Commun. 47 (2009) 7360–7362.
[18] G.H. Lee, J.G. Park, Y.M. Sung, K.Y. Chung, W.I. Cho, D.W. Kim, Nanotechnology 29 (2009) 295205.
[19] H. Liu, G. Wang, J. Wang, D. Wexler, Electrochem. Commun. 10 (2008) 1879–1882.
[20] S. Wang, J. Zhang, C. Chen, J. Power Sour. 195 (2010) 5379–5381.
[21] L. Wang, Y. Yu, P.C. Chen, D.W. Zhang, C.H. Chen, J. Power Sour. 183 (2008) 717–723.
[22] S. Yang, X. Feng, S. Ivanovici, K. Müllen, Ang. Chem. Int. Ed 49 (2010) 8408–8411.
[23] W. Shi, X. Rui, J Zhu, Q. Yan, J. Phys. Chem. C 116 (2012) 26685–26693.
[24] M. Du, C. Xu, J. Sun, L. Gao, J. Mater. Chem. A 1 (2013) 7154–7158.
[25] J.S. Xu, Y.J. Zhu, ACS Appl. Mater. Interfaces 4 (2012) 4752–4757.
[26] Q.Q. Xiong, J.P. Tu, Y. Lu, J. Chen, Y.X. Yu, Y.Q. Qiao, X.L. Wang, C.D. Gu, J. Phys. Chem. C 116 (2012) 6495–6502.
[27] K.S. Novoselov, A.K. Geim, S.V. Morozov, D. Jiang, Y. Zhang, S.V. Dubonos, I.V. Grigorieva, A.A. Firsov, Science 306 (2004) 666–669.
[28] D.R. Dreyer, R. Daniel, R.S. Ruoff, C.W. Bielawski, W. Christopher, Angew. Chem. Int. Ed 49 (2010) 9336–9344.
[29] M.J. Allen, J. Matthew, V.C. Tung, C. Vincnet, R.B. Kaner, B. Richard, Chem. Rev. 110 (2010) 132–145.
[30] D.S. Su, S. Perathoner, G. Centi, Chem. Rev 113 (2013) 5782–5819.
[31] J.N. Coleman, Adv. Funct. Mater. 19 (2009) 3680–3695.
[32] K. Keun Soo, Z. Yue, J. Houk, L. Sang Yoon, K. Jong Min, K.S. Kim, A. Jong-Hyun, P. Kim, C. Jae-Young, H. Byung Hee, Nature 457 (2009) 706–710.
[33] X.S. Li, W.W. Cai, J.H. An, S. Kim, J. Nah, D.X. Yang, R. Piner, A. Velamakanni, I. Jung, E. Tutuc, S.K. Banerjee, L. Colombo, R.S. Ruoff, Science 324 (2009) 1312–1314.
[34] I. Janowska, O. Ersen, T. Jacob, P. Vennégues, D. Bégin, M.J. Ledoux, C. Pham-Huu, Appl. Catal. A: Gen 371 (2009) 22–30.
[35] P. Sutter, Nat. Mater 8 (2009) 171–172.
[36] Z.P. Chen, W.C. Ren, L.B. Gao, B.L. Liu, S.F. Pei, H.M. Cheng, Nat. Mater 10 (2011) 424–428.
[37] W. Baaziz, X. Liu, I. Florea, S. Begin-Colin, B.P. Pichon, C. Ulhaq, O. Ersen, M. Soria-Sánchez, S. Zafeiratos, I. Janowska, D. Begin, C. Pham-Huu, J. Mater. Chem. A 1 (2013) 13853–13861.
[38] W. Baaziz, S. Begin-Colin, B.P. Pichon, I. Florea, O. Ersen, S. Zafeiratos, R. Barbosa, D. Begin, C. Pham-Huu, Chem. Mater 24 (2012) 1549–1551.
[39] W. Baaziz, L. Truong-Phuoc, C. Duong-Viet, G. Melinte, I. Janowska, V. Papaefthimiou, O. Ersen,S. Zafeiratos, D. Begin, S. Begin-Colin, C. Pham-Huu, J. Mater. Chem. A 2 (8) (2014) 2690–2700.
[40] G. Melinte, S. Moldovan, C. Hirlimann, X. Liu, S. Bégin-Colin, D. Bégin, F. Banhart, C. Pham-Huu, O. Ersen, Nat. Commun. 6 (8071) (2015), doi:10.1038/ncomms9071.
[41] O. Gerber, B.P. Pichon, J.M. Greneche, C. Ulhaq, J.M. Greneche, C. Lefevre, I. Florea, O. Ersen, D. Begin, S. Lemonnier, S. Begin-Colin, J. Phys. Chem. C 119 (2015) 24665–24673.
[42] I. Janowska, T. Romero, P. Bernhardt, F. Vigneron, D. Begin, O. Ersen, M.J. Ledoux, C. Pham-Huu, Carbon 50 (2012) 3092–3116.
[43] I. Janowska, S. Zafeiratos O. Ersen, D. Soubane, V. Da Costa, V. Speisser, C. Boeglin, M. Houllé, D. Bégin, D. Plee, M.J. Ledoux, C. Pham-Huu, Nano Res. 3 (2010) 126–137.
[44] R. Yuge, M. Zhang, M. Tomonari, T. Yoshitake, S. Iijima, M. Yudasaka, ACS Nano 2 (2008) 1865–1870.
[45] M.S. Moldovan, H. Bulou, Y.J. Dappe, I. Janowska, D. Begin, C. Pham-Huu, O. Ersen, J. Phys. Chem. C 116 (2012) 9274–9282.
[46] X. Hu, M. Ma, M. Zeng, Y. Sun, L. Chen, Y. Xue, T. Zhang, X. Ai, R.G. Mendes, M.H. Rümmeli, L. Fu, ACS Appl. Mat Interfaces 6 (2014) 22527–22533.
[47] L. Jing, A. Fu, H. Li, J. Liu, P. Guo, Y. Wang, X.S. Zhao, RSC Adv. 4 (2014) 59981–59989.